The role of blood pooling and fibre positioning in Interstitial Photodynamic Therapy

Master's Thesis by
Christopher Orth

In cooperation with Medical Laser Physics,
Department of Atomic Physics,
Faculty of Engineering, Lund University

and

SpectraCure AB

28th of March 2008

LUND UNIVERSITY

ABSTRACT

For the dosimetry of interstitial photodynamic therapy (IPDT), the fibre positioning and the distributed light fluence that activates the treatment are essential. With sufficient supply of oxygen and photosensitiser, the treatment effect depends entirely on the distributed light. By proper dosimetry, the illumination is limited to the tumour and adjacent sensitive tissues are spared.

The fibre positioning was optimised using a fast and reliable stochastic algorithm. In this work, algorithms for a similar optimisation process were analysed, the problem of finding the locations for radioactive seeds in brachytherapy. The differentiating circumstances are that for IPDT a smaller number of sources are used and that there is no requirement on the maximum dose delivered to the tumour. The established fast Simulated Annealing algorithm was settled upon and adapted to fit the special conditions of IPDT. As an alternative, the random step algorithm from the previous thesis by Hjelm and Ericsson [5] was investigated. The new software was implemented into Matlab to allow for further improvements of the dosimetric system. The investigations showed that these two algorithms are fast and reliable and suit the special IPDT problem. Future work should be focused on improving the conditions under which they work, i.e. the objective function.

When blood pooling appears at the fibre tips, light is attenuated and the dosimetry is altered. Therefore, the concept of effective attenuation μ_{eff}, independent of the blood, was investigated. Spatially-resolved measurements confirmed that measurable damping factors can indeed be determined, that vary only slightly with the wavelength. Real-time monitoring and compensation during treatment could therefore be possible. Errors in μ_{eff} of a fibre surrounded by small blood pools were less than 15% with roughly $a_i^{-1} \sim 15 \pm 5 mm^{-1}$ times damping.

SAMMANFATTNING

Interstitiell fotodynamisk terapi (IPDT) är en lovande cancerbehandlingsmetod, bl.a. för prostatacancer. Denna är den idag vanligaste förekommande cancerformen i Sverige, med tio tusen årliga fall av de för båda könen sammanlagda femtio tusen fallen. De inledande kliniska testerna hos SpectraCure AB har påvisat lovande resultat med sjunkande PSA-värden (Prostate Specific Antigen) hos patienterna. Det finns dock fortfarande möjligheter till vidareutveckling av prostata IPDT, framför allt vad avser dosimetrin. IPDT innehåller ingen cancerframkallande radioaktiv strålning, såsom klassisk strålningsbehandling gör, utan bygger på konceptet att ljus aktiverar ett läkemedel på rätt ställen i kroppen. Läkemedlet som kallas fotosensibiliserare, reagerar med naturligt förekommande molekylärt syre, vilket i sin tur angriper tumörcellerna. Eftersom behandlingsdosen utgörs av det tillförda laserljuset från 18 optiska fibrer, så måste dessa utplaceras optimalt.

Positionerna beräknas med hjälp av en intelligent algoritm, som inte bara söker bättre lösningar i sin närmaste omgivning, utan som också med en viss sannolikhet prövar sig fram till det globala optimumet. På detta sätt fungerar Random Step och fast Simulated Annealing algoritmerna, som i detta arbetet anpassats för IPDT. Båda bygger på konceptet att maximera en godhetsfunktion som belönar bekämpning av prostatavävnad, samtidigt som den bestraffar ljus till omkringliggande känslig vävnad. Random Step letar efter bättre lösningar i en stor omgivning och minskar sedan denna successivt. Metoden har visat sig vara snabb och robust, men saknar några egentliga garantier för att den bästa lösningen kommer att hittas. Klassisk Simulated Annealing garanterar däremot att en form av "termodynamisk jämvikt" uppnås, som vid tillräckligt långsamt sjunkande "temperatur" kommer att hitta den bästa av lösningar. Detta tar dock lång tid, varför fast Simulated Annealing valts ut, vilken på ett snabbare sätt konvergerar mot en optimerad godhetsfunktion. Metoderna har visat sig fungera väl efter att de anpassats till det specifika IPDT problemet, det som dock

främst behövs är en problemspecifik optimal godhetsfunktion.

Vid IPDT behandling har man upptäckt att det börjar blöda i prostatan vid några av fiberspetsarna. Detta är främst ett problem för dosimetrin, då blodet absorberar en stor del av behandlingsljuset och kan orsaka ojämn behandling. I syfte att initialt undersöka om dämpningen kan modelleras med faktorer som endast beror av absorption, har spatiellt upplösta mätningar på blodpölar vid fiberspetsarna gjorts. Resultaten visar att den effektiva attenueringen inte påverkas märkbart och att det går att mäta sådana dämpningsfaktorer. Ett litet våglängdsberoende av dessa har även uppmätts, vilket föranleder en önskan för fortsatta studier inom området.

CONTENTS

CHAPTER 1

INTRODUCTION

1.1 Photodynamic Therapy

Prostate cancer is by far the most common cancer type for men and also the most common for both sexes altogether [11], [24]. Photodynamic therapy (PDT) is a fairly new cancer treatment technique, which does neither rely on heating (like hyperthermia, photocoagulation, etc.) nor on ionising radiation (like radiotherapy, brachytherapy, etc.). Instead, the electromagnetic radiation is used for creating oxygen radicals that induce cell damage. Besides light, a photosensitising drug and molecular oxygen have to be present in order for the reaction to take place. The drug accumulates in tumour tissue and is then activated by laser light of matching wavelength. By deciding upon the spatial and temporal light distribution (light dosimetry), the treatment becomes tumour selective.

Of the three reactants (light, photosensitiser, oxygen), the one with the lowest presence determines the treatment outcome. By assuring sufficient photosensitiser and oxygen levels, the light distribution alone can be made decisive for the tissue damage. The light fluence in every point of the tissue can be estimated by performing realtime in vivo measurements. This is how the commercial system for interstitial photodynamic therapy for prostate cancer of the company SpectraCure AB works. The system, which has sprung out of the research in Photonics at the Department of Physics, Faculty of Engineering, Lund University, has at the time of writing recently started its clinical trials and initial results seem to be promising.

1.2   Historical background

Photodynamic therapy pioneered in Germany in the early years of the 20'th century by von Tappeiner [26]. A student of his, Raab, had by coincidence observed how a strike of lightning induced a toxic effect on his chemical experiment [18]. Understanding that the energy transfer from light originated the toxicity, von Tappeiner managed to treat skin malignancies using the photosensitising chemical eosin activated by white light [25]. In the following years, Meyer-Betz examined the photosensitising effect of porphyrin, which is still in use for treatment. He demonstrated general photosensitivity by injecting himself with hematoporphyrin and exposing himself to sunlight, resulting in severe pain and swellings [13].

In 1966, Lipson used PDT for cancer treatment for the first time, but his attempts to cure breast carcinoma showed to be unsuccessful [10]. It was instead Dougherty *et al.* who in 1976 managed to effectively cure skin cancer by PDT, which since then has become a regular treatment modality for this purpose [4]. In the recent years, interstitial photodynamic therapy (IPDT) has been developed for treating inner organs as well. Since the light is delivered through optical fibres stuck into the targeted organ, IPDT also makes it possible to treat tumours of larger size.

1.3   Previous work

The IPDT system of SpectraCure AB was developed in order to provide real-time and individual dosimetry for prostate cancer. It consists of an apparatus containing treatment diode lasers and measurement optics connected to optical fibres. The laser output is controlled by a computer that uses a package of software modules to perform the dosimetry calculations. One of the first versions from 2004, P6, used 6 treatment fibres for the photosensitiser activation. The sensitiser was hydrophilic, which is preferable for superficial treatment (skin, lung, blather, etc.), but when administered orally or intravenously did not effectively penetrate into the centre of the tumour. The current system, P18, see Figure 1.1, has 18 fibres to dose the treatment with the potent and penetrating lipophilic photosensitiser Temoporfin (chemically abbreviated mTHPC). It is only slightly tumour selective, wherefore the light distribution is of outermost importance and the patient has to stay unexposed of strong light for about two weeks.
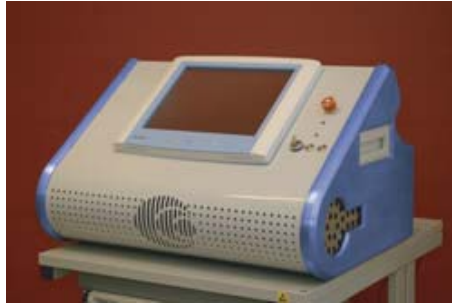
Figure 1.1: The SpectraCure AB setup P18 [6]
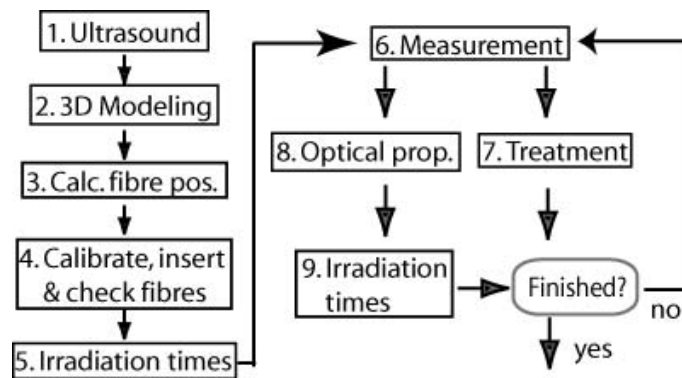
Figure 1.2: Treatment procedure [6]

The treatment procedure is displayed in Figure 1.2. The dosimetry software calculates the positioning of the fibres into the prostate in $3.FibrePositioning$ and the laser irradiation times in $5.Irradiationtimes$. Currently, a software developed by Hjelm and Eriksson for a Master's thesis in 2004 is used for the positioning and this thesis is to a large extent a continuation of their work. Their positioning algorithm is somewhat intelligent in the way it converges towards a good solution and has showed to generate satisfactory results in the time frame of tens of minutes. After the positions have been calculated, the long needles containing the fibres are inserted at the given coordinates. The irradiation times of the individual fibres are then calculated using a Cimmino algorithm to solve a system of inequities, which makes sure that every tumour voxel[1] has a light distribution above treatment threshold.

At insertion and during treatment, blood has been observed to come out of some of the needles. This bleeding itself is not dangerously strong, but if the blood accumulates

---

[1] 3D pixel from the acquired imaging model

at the fibre tips, it will absorb light intended for the therapy. Previous work has stated that a single millimetre of blood is enough to attenuate the light fluence by up to 20 times [23]. Thus, blood occlusion or pooling causes longer treatment times in order to achieve the same dose and most importantly, it alters the distribution and compromises the dose plan. Additionally, the occluded blood, obscures the real-time optical measurements.

1.4   Purpose of the studies

Since the system has undergone major changes, there was need for an investigation and possibly an improvement of the quality of the fibre positioning module. The former module was developed in the software LabView, which is intended mainly for process control and not optimised for numerical computation. To render the possibility to make small improvements to the algorithm's behaviour and to have full control of the calculations, the new version needed to be programmed in Matlab or a similar software. The wish was to reduce the time for the calculation of sufficiently good positions. This would shorten the time in the clinic from acquisition of the 3D tissue model of the patient's prostate to the insertion of the treatment needles. In conclusion, the first aim of the studies performed for this thesis was to find and implement a quick and robust algorithm for the fibre-positioning problem.

The second study reported upon here, has to do with investigation of how blood accumulation at the fibre tips attenuates the light. If attenuation factors can be calculated after just performing some measurements prior to the treatment, these could be taken into account for the calculations of the treatment times of the individual fibres. The result could be a reduction in treatment time and most importantly an improved dose distribution. If a certain fibre showed to only contribute very little to the treatment, because of blood accumulation in front of its tip, the physician might want to adjust its position. This part seeks an answer to the question if blood can be compensated for by multiplying with some attenuation factors and if and how these can be measured.

1.5   Outline of the thesis

The field of photodynamic therapy is diverse and interdisciplinary. Medical physicians, researchers and chemists have the theoretical background needed to understand the biological and chemical processes fully and I will only try to give a brief background about those.

Instead, the focus of this thesis is on the physical mechanisms that are essential. Both the calculations of the fibre positions and the measurements of blood attenuation rely on diffusion theory. The aim of the next chapter, Chapter 2, is to present this theory starting with Photonics in tissue in general. Special attention is turned to the light absorption of blood and the spectroscopic techniques that are needed for those measurements. Chapter 3 attempts to explain some of the basics of interstitial photodynamic therapy, a new and promising treatment modality for solid tumours e.g. prostate cancer. In this context, the theoretical background of the dosimetry calculations needed to understand this thesis, are presented. Chapter 4 and 5 include the methods and the obtained results for the work of this thesis. Chapter 4 presents simulation results for the fibre positioning problem, while 5 includes measurements of how blood at the fibre tip attenuates the light distribution. Finally, in Chapter 6 the results from 4 and 5 are discussed, compared and analysed and suggestions for future work are given.

CHAPTER **2**

BIO-PHOTONICS

2.1 Optical properties of tissue

The structures that are responsible for the optical behaviour of tissue are the cells. Within the cells, the mitochondria (with their irregularly shaped cristae) and lipid vesicles (containing fat which has larger refractive index than water) are major scatter sites. Variations in refractive index cause a highly scattering medium, where the transport of light and heat through it spreads to a larger area. Blood cells and tissue chromophores are major absorbers of visible ($400-750nm$) to near-infrared (NIR) ($750-1400nm$) light. How frequently interactions occur is described by attenuation coefficients, denoted μ. The absorption coefficient μ_a and the scattering coefficient μ_s are summed to the total attenuation coefficient $\mu_t = \mu_a + \mu_s$. The penetration depth of collimated light, the mean free path where it has decreased by a factor $\frac{1}{e} = 0.37$, is $\delta = \frac{1}{\mu}$. These coefficients depend strongly on the wavelength λ and set the limit for the penetration into the tissue.

In biological tissue, scattering is by far larger than absorption, wherefor the area absorbing light increases, generating a more diffuse and weakened effect. Tissue scattering is not isotropic[1], but occurs to a higher extent in the forward direction. The anisotropic scattering factor, the g-factor, describes this phenomenon. Here, -1,0 and 1, signify fully backward, isotropic and fully forward scattering, respectively. In prostate tumour tissue, g typically has high positive values, about $g \approx 0.975$ [3]. The reduced scattering coefficient then becomes $\mu'_s = \mu_s(1 - g)$ instead of only μ_s. For structures smaller than or similar

---

[1]spread equally much in all directions

to the wavelength of the light, isotropic Rayleigh scattering is dominating. It is normally observed for free atoms of nanometre scales; membranes and other small cell structures are responsible for it in the cells. Rayleigh scattering falls off rapidly with the wavelength and is proportional to λ^{-4} [28]. Since it spreads laser light largely, it decreases the selectivity of the treatment and increases the illumination area. Scattering for structures larger than the wavelength, such as the mitochondria is due to Mie scattering. It does not fall off as fast and is proportional to λ^{-b}, where $0.5 < b < 1.5$ [28]. It is forward scattered ($g > 0$), so that the effective scattering of that type is less than for Rayleigh ($\mu_s' < \mu_s$).

2.2   Properties of blood in the tissue

In contrary to tissue discussed in general, the dominating interaction of blood is absorption. The absorption coefficient, μ_a decreases with the wavelength and depends on the amount of the haemoglobin chromophores. In blood occurs both oxygenated haemoglobin, HbO_2, and deoxygenated haemoglobin, Hb. The relative amount of HbO_2 to Hb is typically 75% to 25% in the prostate [22], making it a low oxygenated organ. Because these molecules have different structures, their absorption spectra differ as can be seen in Figure 2.1. A result of this fact for blood vessels is that arteries look brighter than veins, because they contain more HbO_2. Since the scale of the absorption coefficient in Figure 2.1 is logarithmic ($\log_{10}$), the absorptions of hemoglobin decreases rapidly with the wavelength from $400nm$ to $800nm$. Hence, the average length travelled by every photon, the penetration depth with regards to absorption only, $\delta_a = \frac{1}{\mu_a}$, increases strongly with the wavelength if lots of blood is present. Therefore a longer wavelength to penetrate the blood is beneficial.

2.3   Light propagation in scattering media

The light propagation of a fully absorbing medium follows Beer-Lambert's law of exponential attenuation in Eq. 2.1.

$$I = I_0 e^{-\mu x} \tag{2.1}$$

Here, I is the intensity after passing through a medium of length x and with attenuation due to absorption, represented by μ. A similar expression can be derived for a scattering medium, by using the so called diffusion approximation of the radiative transport equation,
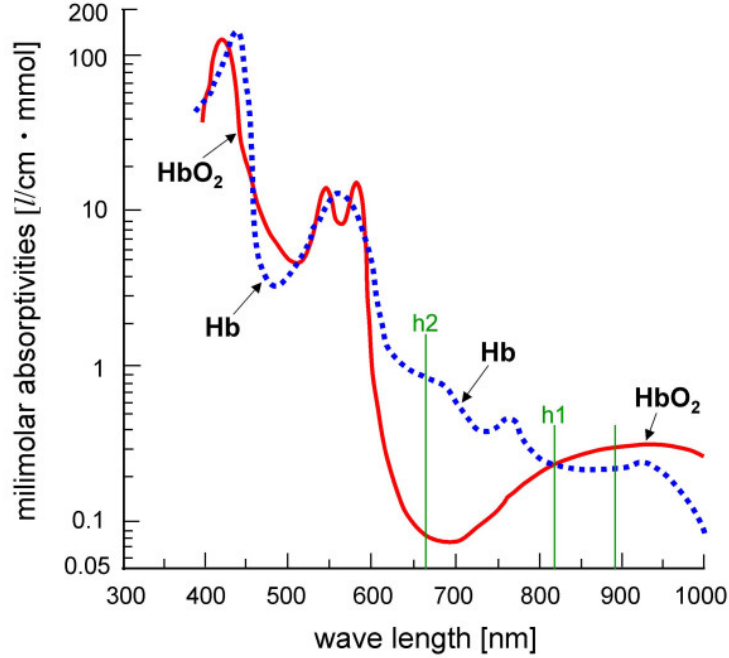
Figure 2.1: Absorption of blood, comparison between oxygenated and deoxygenated haemoglobin [12]

RTE. RTE is a differential equation that describes the change of radiance in a volume element. The terms relate to the flow across a boundary, outgoing scattering, absorption, incoming scattering and flow created by sources within the volume element, respectively:

$$\frac{1}{c}\frac{\partial \mathbf{L}(\mathbf{r},\mathbf{s},t)}{\partial t} = -\mathbf{s}\cdot\nabla\mathbf{L}(\mathbf{r},\mathbf{s},t) - (\mu_s+\mu_a)\mathbf{L}(\mathbf{r},\mathbf{s},t) + \mu_s\int_{4\pi}p(\mathbf{s},\mathbf{s}')\mathbf{L}(\mathbf{r},\mathbf{s}',t)d\omega' + q(\mathbf{r},\mathbf{s},\mathbf{t}) \quad (2.2)$$

Here, c denotes the speed of light, $\mathbf{L}(\mathbf{r},\mathbf{s},t)$ is the light radiance at $\mathbf{r}$ travelling in the $\mathbf{s}$ direction, $d\omega$ is the differential solid angle and μ_s and μ_a are the scattering and absorption coefficients, respectively. The scattering phase function $p(\mathbf{s},\mathbf{s}')$ is the probability to scatter into the $\mathbf{s}$ direction and is for isotropic scattering events simply $\frac{1}{4\pi}$. For anisotropic scattering, a g-factor may be included in the phase function. In such cases, the angle between $\mathbf{s}$ and $\mathbf{s}'$ together with the g-factor indicating some forward scattering usually effects the change in radiance. Since there exists no analytical solution to the RTE in arbitrary geometries, it can only be solved by other means. One method is to solve it by numerical means using a discretization of the radiance. Kubelka-Munk theory, the adding-doubling method and the

discrete ordinates method are examples of this approach. Another approach is to solve it by statistical means using Monte-Carlo simulations. There, the optical properties are used for calculating the probability that a trajectory of photons is absorbed, scattered, etc. The simplest approach to solving the RTE though, is the diffusion approximation.

2.4 Diffusion theory and the diffusion approximation

Under the condition that scattering is the main interaction present, i.e. $\mu_a \ll \mu_s'$, the light propagation might be treated as diffusion. The diffusion approximation is found by expanding the radiance and source term in Eq. 2.2 into spherical harmonics, e.g. for the radiance:

$$\mathbf{L}(\mathbf{r}, \mathbf{s}, t) = \sum_{l=0}^{\infty} \sum_{m=-l}^{l} \sqrt{\frac{2l+1}{4\pi}} \, \psi_{lm}(\mathbf{r}, t) \, Y_{lm}(\mathbf{s}) \tag{2.3}$$

For the first order P_1-approximation, the terms of $l = 0, 1$ are used to express radiance and source in terms of fluence rate $\Phi(\mathbf{r}, t) = \int_{4\pi} \mathbf{L}(\mathbf{r}, \mathbf{s}, t) d\omega$ and radiant flux $\mathbf{F}(\mathbf{r}, t) = \int_{4\pi} \mathbf{L}(\mathbf{r}, \mathbf{s}, t) \mathbf{s} d\omega$, i.e.:

$$\mathbf{L}(\mathbf{r}, \mathbf{s}, t) = \frac{1}{4\pi} \Phi(\mathbf{r}, t) + \frac{3}{4\pi} \mathbf{F}(\mathbf{r}, t) \cdot \mathbf{s} \tag{2.4}$$

The time-dependent diffusion equation is then found under the assumption of an isotropic light source and a time-independent radiant flux:

$$\frac{1}{c} \frac{\partial \Phi(\mathbf{r}, t)}{\partial t} - \nabla \left(D(\mathbf{r}, t) \, \nabla \Phi(\mathbf{r}, t) \right) + \mu_a \Phi(\mathbf{r}, t) = S_0(\mathbf{r}, t) \tag{2.5}$$

Here, S_0 denotes the isotropic light source and D the diffusion coefficient. For any kind of diffusion, a diffusion coefficient is used to describe the speed of the process. When regarding light propagation as diffusion, the diffusion coefficient is formed from the optical properties together with a constant α, so that $0 < \alpha < 1$ describes the time dependence of the diffusion:

$$D = \frac{1}{3(\alpha \, \mu_a + \mu_s')} \tag{2.6}$$

The diffusion equation, Eq. 2.5, is solved by a Green's solution that can be adapted to the amount and types of sources. For a single point-source in an infinite homogenous medium, the following expressions are found in the time-dependent and time-independent case, respectively:

$$\Phi(\mathbf{r}, t) \;=\; \frac{1}{4\pi D c t} \, e^{-\mu_a\, c\, t} \, e^{-\frac{r^2}{4 D c t}} \tag{2.7}$$

$$\Phi(\mathbf{r}) \;=\; \frac{1}{4\pi D r} \, e^{-\mu_{eff}\, r} \tag{2.8}$$

The exponential decay factor in the time-independent Green's solution (Eq. 2.8), is called the effective attenuation coefficient μ_{eff}. It origins from the diffusion coefficient, where the flux has been set to time-invariant ($\alpha = 1$):

$$\mu_{eff} = \sqrt{\frac{\mu_a}{D}} = \sqrt{3\,\mu_a\,(\mu_a + \mu_s')} \tag{2.9}$$

When comparing the time-independent Green's solution (Eq. 2.8) with Beer-Lambert's law (Eq. 2.1), one sees that they differ by the decay coefficient μ_{eff} instead of μ and the $\frac{1}{4\pi D \mathbf{r}}$ term. The latter is the radial term for isotropic scattering as hinted in context with the scattering phase function. The Green's solutions (Eq. 2.7 and 2.8) are not valid close to a source or a boundary ($r < \frac{1}{\mu_a + \mu_s'}$). In prostate tissue, this non-diffusive region is at least a few mm [6].

2.5 Spectroscopic measurements on tissue

Measuring and understanding how the optical properties vary in the tissue is a main aspect of Photonics and Biomedical Engineering. Some of the most popular techniques involve spatially-resolved (SR), time-resolved (TR), frequency-resolved or integrating sphere type measurements. For this work, SR and TR measurements were needed:

SR spectroscopy relies on the measurement of the fluence rate, Φ, at different distances to the source. Theoretically, it does not matter if the source or the detector is translocated, but in reality it is hard to deliver the same power to the sample if the source has been altered. To find μ_{eff}, diffusion theory is used, setting the usual limits to at what minimum distance the solution is reliable ($r > 1mm$). The time-independent Greens-solution (Eq.

2.8) implies that a natural logarithmic plot of the fluence times the radius is a straight line with the gradient μ_{eff}, see Eq. 2.10. Thus, SR measurements at different fibre distances should, if they end up on a straight line, yield μ_{eff} of the sample. In Eq. 2.10, the laser output power, P, and a calibration constant, c, have been included to correct for the laser system.

$$-\ln(\Phi \cdot \mathbf{r}) = \ln(\frac{cP}{4\pi Dr}) + \mu_{eff} \cdot r \qquad (2.10)$$

The method called time-resolved spectroscopy is a powerful tool to estimate the scattering and absorption properties of a sample. Short light pulses are sent into the sample and when exiting they have broadened according to the optical properties of the material that they passed through. By combining the pulse shape to simulations of time-resolved diffusion, matching values of μ_a and μ'_s can be found in databases. The path length of the individual photons are proportional to the their respective arrival time, hence the early photons are ballistic while the tail is made out of slacking photons that have scattered many times. By using more than one wavelength simultaneously, the sample characteristics are easy to obtain.

CHAPTER **3**

IPDT DOSIMETRY

3.1 Prostate cancer

Prostate cancer is the most common type of cancer today [11], in Sweden it is responsible
for nearly 10000 out of a total of 50000 cases (for both sexes) [24]. For men, it is responsible
for 34.6 percent of the incidence and in the last 20 years there has been an annual increase
of 2.9 percent [24]. The disease and its increase are strongly age related, 96.4 percent are
above 50 years of age and almost half of them are more than 65 years old [24]. Symptoms
include pain, difficulty in urinating and erectile dysfunction and there is a risk that the
cancer may spread to other organs. Prostate cancer is most often discovered by performing
a rectal examination or by blood screening tests to find out the level of PSA, Prostate
Specific Antigen . High PSA indicates a high activation of the prostate immune system and
is thus a disease indicator [27]. However, the PSA level may vary from patient to patient,
wherefor it should not alone be used to determine if and what kind of treatment to give
[27]. Another reason for being careful with giving treatment is that prostate cancer is not
necessarily a fast growing cancer, wherefor many incidences are not even discovered or will
not cause any problems until the carrier dies of other causes. Some incidences though, can
be very aggressive and spread, but it is very difficult to predict if that will be the case [14].
A prostate biopsy examination is an established way to confirm the incidence of the disease
if the PSA was high. In such cases, x-ray screenings, etc. are needed to determine if the
cancer has spread. Even though the carcinogenic tissue does not occupy the entire prostate,
the full organ is normally treated as tumour tissue, since microscopic cells of tumour tissue

are hard to distinguish and impossible to treat.

Common treatments include surgical removal of the organ, radiotherapy, hormonal therapy or a combination of several treatment modalities. A general problem is that cancer treatments are not always selective of certain organs. In the case of the traditionally most common radiotherapy procedure, the external beam, a large dose will also be given to adjacent healthy tissue. Particularly fragile surrounding organs include the rectum, the upper and lower sphincter muscles and their respective nerve bundles and the urethra. In external beam radiotherapy of internal organs, MeV X-rays from one or several beams penetrate through the patient into the location of treatment. These high energy photons ionise the tissue along their path, so that the penetrated tissue receives at least the same amount of dose as the location of interest receives (from the same beam). Another radiotherapy modality that is popular for prostate cancer treatment is brachytherapy, where many small radioactive seeds (up to 100) are planted into the tumour. The seeds emit the γ-radiation that ionise the tissue and are planted by a surgical technique using long needles. The same surgical needle insertion is used in Interstitial Photodynamic Therapy (IPDT) on the prostate, but for an entirely different purpose. In this case, optical fibres are put through the needles to deliver visible (or NIR) laser light, i.e. non-ionising radiation, which by itself does not harm the tissue.

3.2   Mechanisms in Photodynamic therapy

In Photodynamic Therapy (PDT), a photosensitiser becomes activated by light and then forms toxic reactants, which cause cellular damage. The energy transfer taking place is studied in atomic physical terms, see Figure 3.1. When the photosensitiser's absorption band is matched by the light at $652nm$, it is excited from the ground state, the singlet state referred to as S_0, into a higher singlet state, S_1. There, it can relax back into the ground state or it can transfer its energy into an excited triplet state, T_1. This state is meta-stable since the transition to the ground state is not allowed due to the conservation of spin.

There are two different mechanisms by which the excited triplet state photosensitiser can interact with biomolecules. In the so-called type I reaction, a transfer of an electron or a hydrogen ion from the photosensitiser forms reactive radicals. This happens either directly or indirectly via surrounding substrates. These radicals usually react with oxygen to form ROS, reactive oxygen species. The ROS can oxidize the ground state photosensitiser, leading to
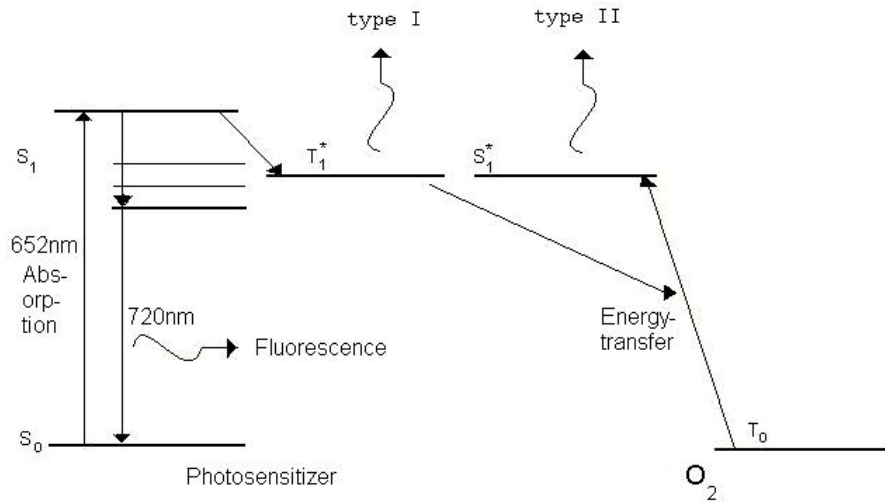
Figure 3.1: Simplified energy-level diagram indicating the transfer from the photosensitiser (mTHPC) to singlet oxygen $^1O_2$

its consumption. This is referred to as photobleaching, implying that the irradiation causes a bleaching (decrease) of photosensitiser.

It is the type II reaction that is believed to cause the most of the cell damage for the treatment [6]. The photosensitiser in the excited triplet state, exchanges energy and electron spin with ground state molecular oxygen. The photosensitiser ends up in the singlet ground state and is thus again available for new reactions. The oxygen ends up in an excited singlet state of long natural lifetime, making it highly reactive. Since its diffusion length is very short, the photosensitiser must already be localised at the structure targeted for treatment. Where the photosensitiser locates depends on its chemical structure. Hence the choice of photosensitiser is dependent of the chemical environment of the targeted organ.

The damage caused by singlet oxygen results from a combination of direct cell death, vascular damage and immune response. Direct cell death is caused by apoptosis and necrosis. Apoptosis is the natural process of cellular suicide, which prevents inflammation etc., and necrosis is the unprepared cell death. Vascular damage causes indirect cell death, since it cuts of the circulation to the tumour, preventing its re-growth. Unfortunately, it also leads to hypoxia[1] making the treatment inefficient. Normally, an oxygen supply that is

---

[1] insufficient oxygen supply

sufficient for treatment is assumed, but if this is not the case, the treatment can be split into fractions to give time for reoxygenation [15]. Therefore, the oxygen level should be monitored during treatment. The immune response is characterised by an activation of the anti-tumour immune system through the release of antigens. This is significant for the long-term effect to prevent re-growth of the tumour and there are actually therapies that depend strongly on this immune response, such as thermotherapy (where tumour cells are killed by heating). Since the photosensitiser does not accumulate inside the cell nucleus, there is actually no direct damage on the DNA. Thus there is very little risk of causing unwanted mutations etc, wherefor PDT is not considered carcinogenic.

3.3 IPDT on the prostate

The presurgical dosimetry uses a 3D model from a transrectal ultrasound imaging procedure (TRUS) as can be seen in Figure 3.2 a). After the surgeon has marked out the boundaries of the different tissues for the IPDT system, the positions and a dose plan are calculated. Since the light power of the individual fibres are kept at constant, it is only the time of illumination that makes up the dose. The dose to the patient is in this case expressed in energy per area (instead of energy per mass) and called light fluence, by convention Ψ. In Eq. 3.1, Ψ is the fluence in $\frac{J}{m^2}$, Φ the fluence rate in $\frac{W}{m^2}$, t the time in s, and n_{fibres} the number of fibres.

$$\Psi = \sum^{n_{fibres}} \Phi_i t_i \tag{3.1}$$

The technique for the physical positioning of the needles has been adapted from brachytherapy, where the radioactive seeds are planted into the prostate. After the positioning the coordinate calculations, the physician still has the possibility to shift the positions slightly, e.g. if the positions are too close to the gland boundary or to sensitive adjacent tissue. To place the needles correctly according to the given coordinates, the surgeon inserts the long needles through an external hole-matrix into the prostate, see Figure 3.2 b). The needles contain the optical fibres connected to diode lasers. While pushing the needles through the hole matrix the surgeon is guided by the real-time TRUS imaging. Once in place, the actual laser duration times are calculated along with a dose plan that is used if accepted by the physician.
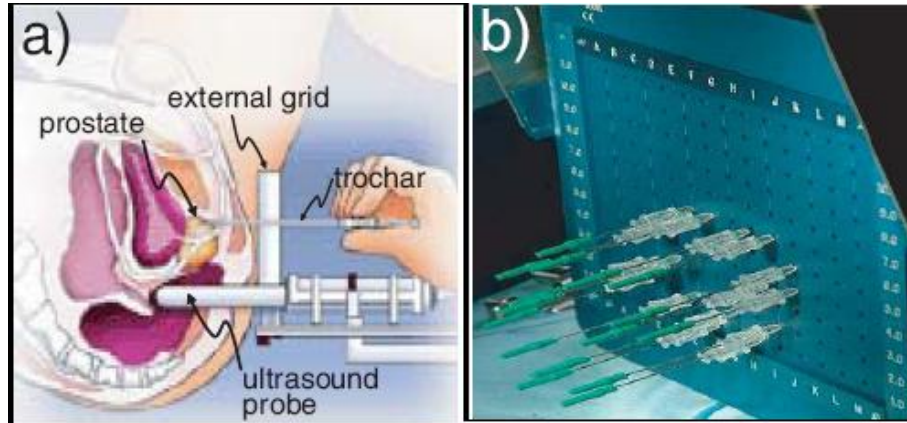
Figure 3.2: IPDT Treatment [6]

Stresses and strains will occur at any interstitial treatment using needles for the placement of fibre optics. If too large they might give rise to initiated bleeding, haemorrhage. The actual illumination may also induce some heating when the absorption excites vibrational or translational modes in the molecule or when inelastic scattering occurs. If sufficient energy is transformed into heat, hyperthermia may induce cell death if a temperature somewhat higher than regular is held for sufficiently long. In the case of short but strong temperature rise, blood will coagulate after a few minutes at around $65°C$.

3.4   Optimal fibre positioning

It is a poor strategy to place the fibres close to the boundary of the prostate, since the light might be absorbed by other tissues. The positions can not be too close to sensitive tissues, wherefore positions at the top and the bottom of the prostate, close to the sphincters, should be avoided. The irregular shape of the prostate in combination with the certain criteria of sensitive surrounding tissues, makes the problem quite complex. The resolution of the acquired Ultrasound images, the human factor of surgical positioning and the stability of a needle position within the prostate all set a limit to the resolution of our prostate model. Better than a mm accuracy is not realistic. Using a mm as voxel size, there are about $n_{voxels} = 36000$ voxels in an Ultrasound 3D model of a $40 \times 30 \times 30mm$ prostate (which fits the measures of actual prostate 3D models). The number of unordered and unique combinations for n_{fibres} fibres and n_{voxels} voxels can be calculated as:

$$C = \left(\begin{array}{c} n_{voxels} \\ n_{fibres} \end{array} \right) = \frac{n_{voxels}}{n_{fibres}!(n_{voxels} - n_{fibres})!} \tag{3.2}$$

For $n_{fibres} = 18$ this number is too large to iterate through, $C \sim 10^{66}$. The calculation efficiency of the computer sets the ultimate limit while the speed of the software most often sets the practical one. On a regular computer, Matlab works at about 10^6 calculations per second. To iterate through all problems would thus take $t = 10^{66-6}s = 10^{60}s \sim 10^{52}y$. Instead, one has to satisfy with finding an acceptably good solution in a fixed amount of time, rather than the best possible solution.

3.4.1 Objective function

To quickly evaluate the quality of a combination of fibre positions, an objective function can be used. In this case, the objective function is multi-objective, since it rewards tumour tissue illumination and punishes light distributed to adjacent sensitive tissues. One type of objective function finds the fitness value, f, by summing the fluence of the voxels, $\Psi_{i,k}$, multiplied with some tissue specific weight factor, w_k, as seen in Eq. 3.3.

$$f = \sum_{k=1}^{n} \left[\sum_{i=1}^{N_k} w_k \Psi_{i,k} \right] \tag{3.3}$$

Here, k sums over all of the n tissue types and i over N_k voxels within that tissue type. The tissue weights, w_k, can be varied to achieve the wanted characteristics of the algorithm, e.g. by adding more weight to reward or to punish. Another type of objective function is the least squares function, which squares the difference to a tissue specific threshold dose, Ψ_k^{th}, as seen in Eq. 3.4.

$$lsq = \sum_{k=1}^{n} \left[\sum_{i=1}^{N_k} w_k (\Psi_{i,k} - \Psi_k^{th})^2 \right] \tag{3.4}$$

3.4.2 Optimisation Algorithms

There are several types of optimisation algorithms that find an extremum on a convex surface, avoiding the (brute force) exhaustive approach. Here is a list of some of the most

popular ones for brachytherapy:

Deterministic algorithms

Deterministic means that the result will always be the same (under the same conditions) since there is no randomised behaviour that controls the path from the starting point to the end point.

- **Deterministic Step**: A faster and more sophisticated approach than the systematic search of all possibilities is by taking steps, e.g. towards the strongest gradient.

- **Linear programming**: If the problem can be formulated as a linear programming problem (many sophisticated problems can indeed), than this is the quickest way of solving it since this is the straight forward mathematical solution (using matrices)[1].

- **Integer programming**: A variant of linear programming that uses only discrete values [21].

- **Greedy heuristic using adjoint functions**: Greedy algorithms make only local optimum choices and these can predicate on a priori ranking of locations. In brachytherapy adjoint functions are popular to in advance make a map of how good certain locations are to place a seed in, based on the proximity to adjacent tissues, etc [29].

Stochastic algorithms

Random number generation determines the result, which in general is a fast way to find sufficiently good solutions. One can not expect to actually find the global optimum in a short time period, but the solution should converge towards it.

- **Random Search**: The pure random search should result in a Gaussian distribution of fitness values (if unbiased). More sophisticated random algorithms have some decisions determined by probability, e.g. if to move towards the direction of the strongest gradient.

- **Random Step**: Steps are taken in the direction of minima when navigating on the surface of solutions. In purpose of not getting stuck in a bad local minimum, there is a (low) probability of trying out disadvantageous steps. These "uphill" steps redirect into "deeper valleys".

- **Simulated Annealing**: Simulated Annealing is an analogue to metallurgic cooling by reaching thermodynamic equilibrium. Disadvantageous random steps are allowed with a probability according to the Boltzmann distribution, where the objective function is the analogue to the energy.

- **Genetic Algorithm**: This algorithm mimics the evolution using the objective function as the analogue to the probability of reproduction [6].

Simulated Annealing Algorithm

The Simulated Annealing (SA) algorithm has among other things been used to solve the classical travelling salesman problem, where the travelling salesman wants to find the shortest path to travel ones through a large set of cities on a map. It can also be used for designing integrated circuits to minimise interference among connecting wires [8]. Further, it is in use in brachytherapy, where it has shown to be superior to geometrical optimisation, i.e. spreading the radioactive seeds as much as possible [16]. The above examples have in common that brute force would take too long to be a realistic alternative and that they are subject to some individual and complicated objective function.

SA is a thermodynamic analogy to the way that metals cool and anneal [2] (thus the name Simulated Annealing) or the way that liquids freeze and crystallise. When the temperature of a liquid is high, molecules move almost freely with respect to one another. When cooled down slowly, they find the energetically best configuration and line up in an ordered fashion to form a crystal. Cooling of a liquified metal works similarly, but when it cools too fast, it is "quenched" meaning that it ends up in a state of higher energy than the equilibrium. In SA, the energy is the objective function and an improvement is a negative energy difference, $\Delta E < 0$. In that case the configuration change is always accepted independent of the temperature. A positive change however, is accepted only with a probability according to Eq. 3.5, similar to the Boltzmann distribution.

$$P(accept \Delta E) = \left\{ \begin{array}{ll} 1 & if \quad \Delta E < 0 \\ e^{-\frac{\Delta E}{kT}} & if \quad \Delta E > 0 \end{array} \right. \tag{3.5}$$

There are four main ingredients of the SA algorithm, developed by Metropolis [17], [8], [20]:

---

[2] heat treatment that causes the atoms to diffuse within a solid material

1. The possible configurations of the system

2. Random generator to make changes to the system, accepting the changes is optional

3. Fitness function to minimise, analogue to the energy of a thermodynamic system

4. Control parameter T, analogue to the temperature, which is lowered according to an annealing schedule: After a certain amount of improvements or after a certain amount of changes, T decreases by some factor, e.g. linearly by a factor lower than 1 or logarithmic to increase the frequency of iterations towards the end. Which one is preferable should be decided upon experimentally [17].

CHAPTER 4

OPTIMAL FIBRE POSITIONING

4.1 Methods

The purpose of the dosimetry is to accomplish treatment for as many of the tumour tissue voxels as possible, while minimising the dose to other voxels, i.e. to spare sensitive tissues. We define treated voxels as voxels with a dose above the treatment threshold of that tissue type. As mentioned in the Introduction, this is done in two steps at SpectraCure AB. First the optimal fibre positions are computed and after insertion, the illumination times of the individual fibres are calculated. It is the Cimmino algorithm [2], [6], [7] that assures that all tumour voxels actually fulfill the treatment condition. The positioning software assumes the same illumination times for every fibre and is thus essential for keeping these durations similar and thereby keeping the treatment as short as possible.

4.1.1 Quality of the solution

To compare the quality of an algorithm and its solutions a number of quantities were observed in the following order:

1. The fitness value and how it converges to a better solution.

2. Visual observation of how evenly spread positions become and how their summed fluence covers the prostate. The summed fluence is not included in the results, since they did not supply much additional information.

31

3. The result of the Cimmino dosimetry in terms of how similar the laser irradiation times become and how satisfactory the dose-volume histograms (DVHs) appear [19]. For a treatment plan a DVH is calculated using the doses, i.e. the fluence given. DVH is a concept from radiation therapy treatment planning to visualise, how many of the voxels that receive treatment dose e.g. 95% of tumour voxels receive at least 100% threshold dose. See Table 4.1 for the evaluation criteria.

4. The Matlab run profiler giving information about the individual running times of the code.

Table 4.1: Tissues threshold for treatment

Tumour tissue	$\geq 95\%$ of voxels receive $\geq 100\%$ dose
Urethra	$\leq 90\%$ of voxels receive $\leq 100\%$ dose
Rectum	$\leq 80\%$ of voxels receive $\geq 100\%$ dose
Upper sphincter	$\leq 80\%$ of voxels receive $\leq 100\%$ dose
Lower sphincter	$\leq 50\%$ of voxels receive $\leq 75\%$ dose

4.1.2   Objective function

One idea for calculating the fitness value is to use all tumour tissue voxels by summing up all their fluence values, i.e. taking $N_{k=2}$ to be all tumour voxels in Eq. 3.3. Previous work stated that this is not a great idea, since it results in that voxels of too low fluence become compensated for by some voxels of very high dose [5]. That leads to clustering[1] of the fibre tips, so that a large amount of tumour voxels do not meet the treatment criteria. Instead, only the fraction of the tumour voxels with the lowest doses are summed, empirically 25% was found to be sufficient. For the healthy tissue, the voxels of highest dose should be minimised to reduce strong light to sensitive regions and to thereby avoid damage. One problem is that the Ultrasound 3D model can have different ratios of healthy to tumour tissue depending on the size of the Ultrasound images and the geometry of the prostate. This concern was dealt with by again only including a fraction of the voxels, 30% was found to be suitable for the Ultrasound 3D models that were used.

Using the presumption that t is the same for all fibres, the fluence rate $\Phi_{i,k}$ from Eq. 3.1, can be used for calculating the fitness value, f. With the use of Eq. 3.3, the objective function becomes Eq. 4.1. It has been separated into two parts to better illustrate how the

---

[1]accumulation in adjacent positions

tumour tissue is rewarded while the other tissues are punished. Here, k denotes the tissue type, w_k the tissue weight and N_k are the fractionised number of voxels according to Table 4.2. The percentage of total voxels have been taken from the 3D model that will be used for algorithm comparison in this thesis.

$$f = \left[\sum_{i=1}^{N_k} w_k \Phi_{i,k} \right]_{k=2} + \sum_{k=3}^{6} \left[\sum_{i=1}^{N_k} w_k \Phi_{i,k} \right]_k \tag{4.1}$$

Table 4.2: Exposed tissues and their relative weight

	Tissue type	k	Voxels in f	% of total voxels	w_k
Normal tissue	Other	1	none	80.58%	0
Tumour tissue	Prostate	2	25% lowest	15.40 %	1.0
Sensitive tissue	Urethra	3	30% highest	0.62 %	-1.5
	Rectum	4	30% highest	3.26 %	-1.7
	Upper sphincter	5	30% highest	0.06 %	-2.0
	Lower sphincter	6	30% highest	0.08 %	-1.0

Since the rectum is a large organ, it automatically contributes to a large extent to the fitness value. It is also very sensitive and thus receives a weight that is actually high with regard to its high amount of voxels. Urethra is known to heal quickly and has thus a small weight with regard to its low amount of voxels. The main reason to keep the positions away from the urethra is that a surgical injury there might get complicated because of the urine it withholds. The sphincters are muscles that surround the urethra and are used to control the flow of urine. They are not that sensitive, but injuries must be prohibited because of their essential function, especially for the lower sphincter. The values of w_k were already given from empirical estimation and experience at SpectraCure AB, but could be altered to improve the positioning.

Other possibilities of constructing the fitness function have been tried out. The least squares method of Eq. 3.4 summed instead the differences to the threshold value for treatment, $50 \frac{kJ}{m^2}$. The method was abandoned since it gave rise to very large variation of the fitness value and positions that did not spread evenly across the prostate. To compare the quality of solutions based on the objective function, random search solutions were developed, using the same parameters. Only if the calculated fitness value was one of the best solutions, it was considered satisfactory.

4.2   Software

4.2.1   Input

The following input was supplied for all algorithms:

- The Ultrasound 3D model which is a cube matrix of 60 - 80 voxels in each direction. Every voxels has a tissue characterisation value according to k-sequence in Table 4.2: fileName = 'classification3DModel'

- Homogenous optical properties:
  $\mu_a = 0.6 cm^{-1}$
  $\mu'_s = 10 cm^{-1}$

- Treatment specifics:
  $n_{fibres} = 18$
  $\Phi_{max} = 1.2 \cdot 10^6 \frac{W}{m^2}$
  $P_{max} = 0.15 mW$
  voxelSize = $1mm$

- Minimal distance to side of tumour and between 2 fibres respectively. minDistToSides is used both when randomly choosing initial positions and when moving by small steps, while minDistBetweenFibres is only used when randomly choosing initial positions:
  minDistToSides = $1mm$
  minDistBetweenFibres = $1mm$

- Tissue weights are the weights for the fitness value calculation in k-sequence:
  $w_k =$[0 1 -1.5 -1.7 -2 -1]

- Tissue Voxel Fractions:
  FTTF = 0.25 (Fraction of Tumour Tissue in Fitness function)
  FSTF = 0.30 (Fraction of Sensitive Tissue in Fitness function)
  tissueVoxelFractions =[0 FTTF FSTF FSTF FSTF FSTF] (in k-sequence)

4.2.2   Fitness value

Using the time-independent Greens solution for the diffusion equation, Eq. 2.8, under the assumption of isotropic μ_{eff}, calculated using Eq. 2.9 from the input above, a discrete

fluence distribution for one single fibre is initially calculated in every program. This matrix is of sufficient size to be centred everywhere in the tissue model, i.e. double the dimensions of the 3D model. With the use of that matrix, the summed fluence of many (18) fibres is easily calculated. That summed fluence is then turned into a fitness value with Eq. 4.1. This fitness value calculation is quick since only a fraction of the voxels are used and all the regular tumour tissue voxels are sorted out.

For comparisons a large set of fully random distributions were made on the same 3D model that will be used to present the results upon for the other algorithms. In Table 4.3 the statistics are presented and in Figure 4.1 the distribution is shown for a 6 hour run.

Table 4.3: Statistics from random distributions

n	58076
t	6h = 21600 s
μ	-4.4586e+006
σ	2.6216e+006
min	-1.9741e+007
max	2.9715e+006
$\mu + 2\sigma$	7.8458e+005
$\mu + 3\sigma$	3.4062e+006

4.3   Random Step algorithm

Initially, the Random Step algorithm, as described in general in the thesis from 2004 [5], was implemented into Matlab as one option for the final software. This algorithm builds on random configuration and random relocation of the 18 fibres within the prostate. As
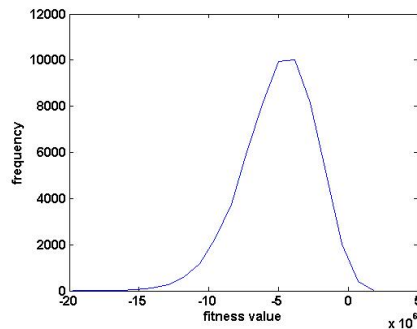

Figure 4.1: Random distribution of fitness values

Method	n	iterations	$\mu(t) \pm \sigma(t)$	$\mu(f) \pm \sigma(f)$
Old	5	900	(approx 1h)	$(-1.532 \pm 0.729) * 10^6$
New	5	900	$661 \pm 21s$	$(5.943 \pm 0.369) * 10^6$
New	5	300	$205 \pm 7s$	$(3.059 \pm 0.816) * 10^6$

Table 4.4: Comparison of old and new Random Step

the name implies, the configuration is manipulated by transforming each position by small random steps. The intelligence of the algorithm lies in how the size of the steps are chosen. The maximum step size is subsequently decreased to find a local minimum on the surface of fitness values of possible configurations. In this sense it is similar to the SA method. Each step size is performed a large number of times, i.e. there are many random step reconfigurations on each step size setting. Every reconfiguration is evaluated by computing the fitness value and only those where an improvement was made are kept. Thus, the system relies on comparing the quality of the current with the previous reconfiguration. The following algorithm specific input was supplied:

- Iteration cycles with the following step sizes:
  stepSize = [5 3 1] voxels

- Number of iterations performed to improve randomly chosen initial values by moving by small steps (1 iteration takes $\approx 0.85s$):
  nIterationsPerRun = 300

The temporal behaviour of the the Random Step algorithm with regards to fitness values typically looks like in Figure 4.2. The fitness values found are in the magnitude of 10^6 and the convergence towards a better solution seems to be very stable with only occasional dips. In the following figure, Figure 4.3, the actual positions are drawn, but unfortunately only a 2D slice of the 3D image can be displayed. In the last figure used to present the results, Figure 4.4, the dose-volume histogram is shown. These results will be more thoroughly discussed in the next chapter.

To compare the new Random Step with the currently used [5], 1h simulations were made with the old software and there positions evaluated with the new. A main difference of the versions are the way the fluence is calculated and that the new version uses step sizes [531] instead of [321]. The positions seems to be more evenly spread out with the old version, but the fitness values were easily improved with the new. The results are summarised in Table 4.4.
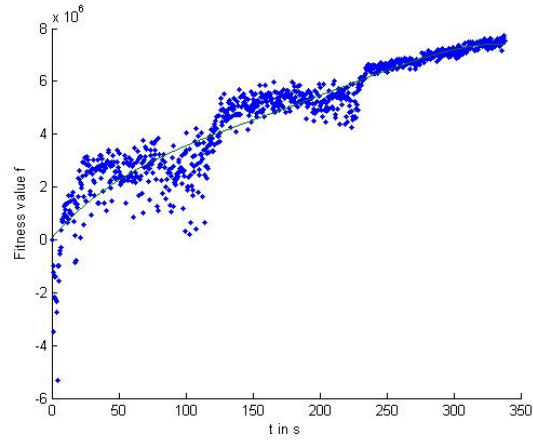
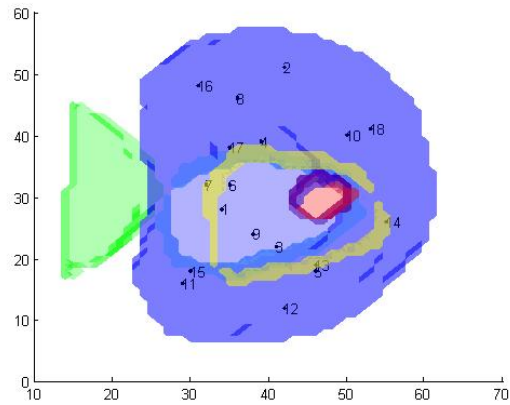Figure 4.2: Time convergence of fitness function from Random Step algorithm

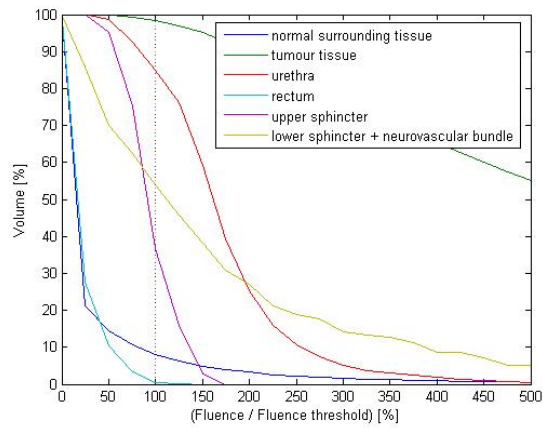Figure 4.3: Prostate with positions from Random Step algorithm

Figure 4.4: DVH from Random Step algorithm

4.4 Simulated Annealing

SA algorithms differ in how their annealing schedules are implemented. The original one by Kirkpatrick et al. [8] is the linear one where the temperature is multiplied with a factor of 0.9 at each iteration, i.e. $T_{i+1} = 0.9 \cdot T_i$. In [20] a second alternative schedule is discussed, which successively increases the multiplication factor to give the temperature $T_{i+1} = T_i \frac{ln(i+1)}{ln(i+2)}$. When tried out, this did not seem to improve (as is also stated in [20]), wherefor it was quickly abandoned. In [17], other annealing schedules are discussed but they have in common that they use a lot of computation power on ensuring the reach of equilibrium. This is caused by the fact that they remain at a constant temperature for long and try out many reconfigurations. According to [17], defining N as the number of possible fibre locations, one should stay at constant T for $100N$ tried reconfigurations or $10N$ successful reconfigurations to ensure equilibrium. Limiting N to a lower value seemed like a good idea because of the computational demand and after extensive trial and error, it was settled at $10 \cdot n_{fibres}$ and $1 \cdot n_{fibres}$, respectively. The results are presented in Figures 4.5, 4.6 and 4.7 in the same fashion as for Random Step. The following algorithm specific input was supplied:

- Maximum step size:
  scaleParameter = 3 voxels

- Original annealing scheme suggested by Kirkpatrick et al., other possibilities available:
  nRandoms = 100 (Number of random configurations to use for setting T_0 as the mean change in fitness value)
  multiplierT = 0.9 (Multiplication factor to decrease T with)

- Breaking the entire computation when converging towards optimum, break if ratio between fitness values is less than convergenceThreshold for consequtivesForConvergence number of times:
  convergenceThreshold = 0.001
  consequtivesForConvergence = 3

- Reconfigurations before breaking an iteration at a constant temperature nImprovementsPerIteration = $1 \cdot n_{fibres}$
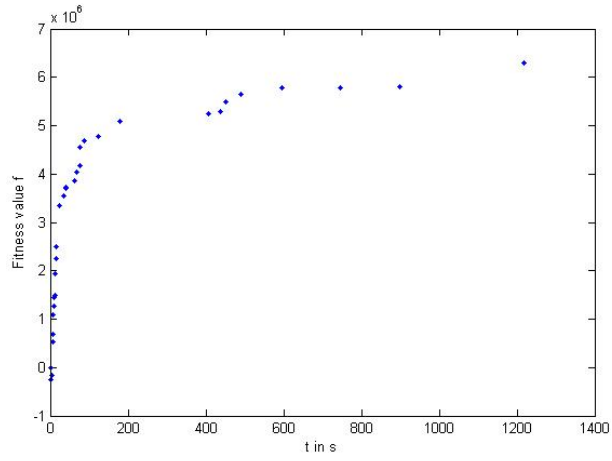 nConfigurationsPerIteration = $10 \cdot n_{fibres}$

Figure 4.5: Time convergence of fitness function from Simulated Annealing algorithm
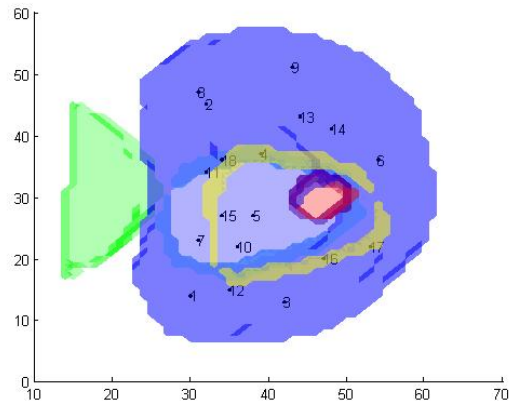

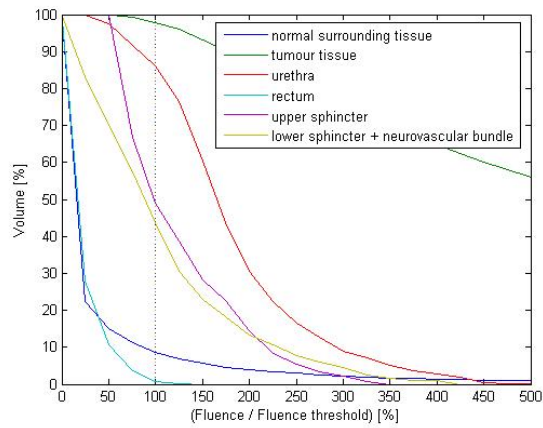Figure 4.6: Prostate with positions from Simulated Annealing algorithm

Figure 4.7: DVH from Simulated Annealing algorithm

4.5   Fast Simulated Annealing

The fast Simulated Annealing algorithm (fSA) iterates a single time on every temperature step, but takes many more steps instead. Thereby it is much quicker in improvements, but at least theoretically not as stable [16]. Regular SA statistically assures that thermal equilibrium has been reached, but tends to be too slow for practical cases [16]. The fast annealing scheme that gave the best solutions is very basic: $T_i = \frac{T_0}{i+1}$. Other possibilities include $T_i = \frac{T_0}{i^{0.6}}$ [9]. The former was used and takes the following input data:

- Maximum step size:
  scaleParameter $= 3$

- Number of random configurations for setting T_0 as the mean change in fitness value:
  nRandoms $= 100$

The results are presented in Figures 4.8, 4.9 and 4.10 in the same fashion as for former two. Notice that in Figure 4.8, a fitness value above $6 \cdot 10^6$ was reached within $150s$, while the regular SA needed $600s$ for the same task. The (low) frequency of the data points in Figure 4.5 is just due to the (external) registration of these values.
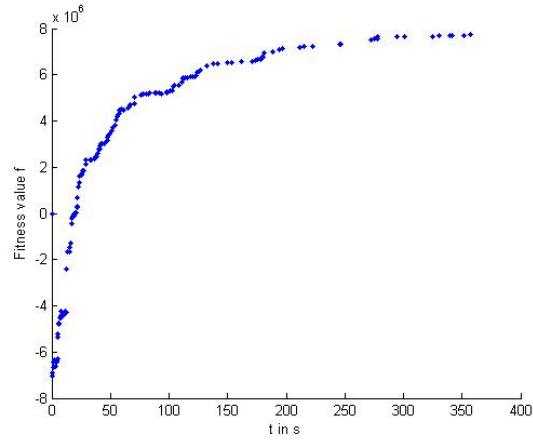
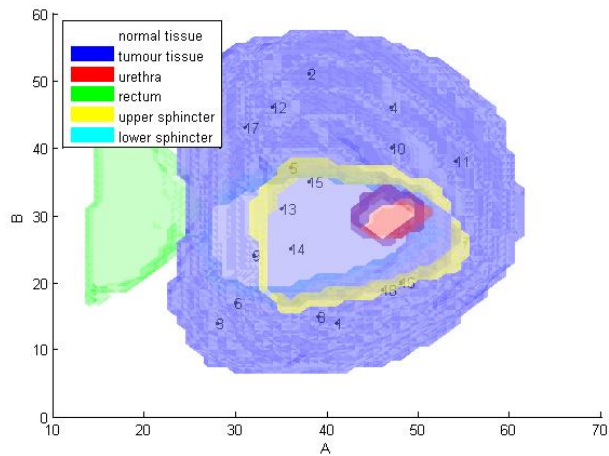Figure 4.8: Time convergence of fitness function from fast Simulated Annealing algorithm

Figure 4.9: Prostate with positions from fast Simulated Annealing algorithm
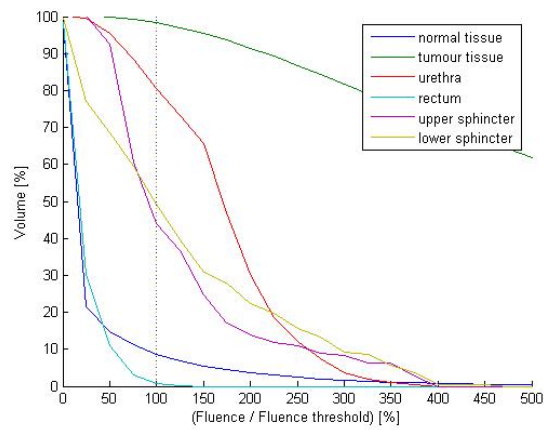

Figure 4.10: DVH from fast Simulated Annealing algorithm

CHAPTER **5**

FIBRE TIP BLOOD POOLING

5.1 Study objectives

To better understand the effects of blood occlusion, it was investigated how the light transmission varies with the amount of blood surrounding the fibre tip. The problem is approached with the assumption that the blood pooling adds some damping factors that are only dependent on the blood absorption and not on the scattering properties. This assumption is here investigated experimentally in purpose of finding some damping factors for different wavelength and base a conclusion on that.

5.2 Experimental Setup

A $600ml$ phantom resembling the prostate was used, containing $570ml$ water, $20ml$ intra lipid at $20mg$ fatty acid per ml, and $2.5ml$ of bovine blood. A single detection fibre and a single light emitting fibre of outer diameters of $0.8mm$ were used for the spatially-resolved measurements. Instead of blood pools of different volumes, solutions of different concentrations of blood to water were poured into the thin glass tubes that were sealed at the bottom by melting them together. The tubes had an inner diameter of $1mm$, wherefore a $0.5mm$ blood attenuation distance was assumed. The fibres were placed parallel into the prostate phantom at the same hight to hold the validity of the diffusion approximation. A high-power white light lamp emitting all the way from infra-red to ultra-violet supplied the light distribution which was measured at $350 - 1030nm$ with a spectrometer. Three blood

Figure 5.1: Spatially-resolved measurement
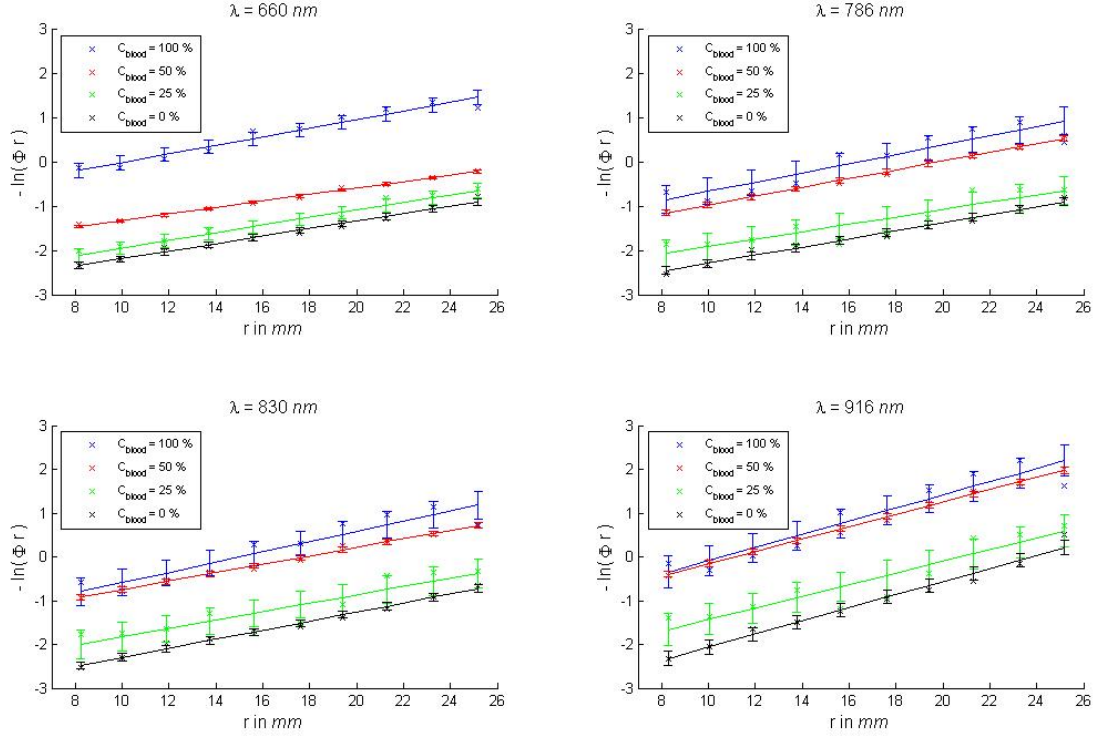
concentrations ($C_{blood} = 100\%, 50\%, 25\%$) and pure water ($C_{blood} = 0\%$) were measured on. Figure 5.1 displays these measurements at four wavelengths of the spectrum, $660nm$, $786nm$, $830nm$ and $916nm$. The wavelengths presented here were chosen because of the possibility to get reference values on those wavelength with the aid of time-resolved spectroscopy, which are shown in Table 5.1. Here, Eq. 2.9 was used to get μ_{eff} out of μ_a and μ'_s. The SR data is presented as the data points in Figure 5.1 on a logarithmic plot of the the fluence rate, Φ, times the distance between the fibres, r. They were fitted using the linear polyfit command in Matlab.

Table 5.1: Optical properties of phantom in cm^{-1} from TR measurements

	μ_a	μ'_s	μ_{eff}
660 nm	0.020	6.3	0.616
786 nm	0.041	5.7	0.840
830 nm	0.048	5.0	0.853
916 nm	0.106	4.7	1.236

$$-\ln(\,\Phi \cdot \mathbf{r}\,) = \ln(\,\frac{c\,a_i\,a_j\,P}{4\pi\,D\,r}\,) + \mu_{eff} \cdot r \qquad (5.1)$$

To use diffusion theory on the experiment, Eq. 2.10 was extended to include the blood attenuation coefficients, a_i, for the source and a_j, for the detector, see Eq. 5.1. The detection fibre had no blood, i.e. $a_j = 1$. Further, the calibration constant, c, was dropped since only relative measures were of interest. Finally, the output power, which can differ among the measurements, was dealt with by normalisation using the average transmitted power (without blood) of Table 5.2. That measurement was performed with a power calibrator that was coupled to an integrating sphere, which consists of a hollow sphere with a slit.

Table 5.2: Average transmitted power per second, $a_i \cdot P$, in $\frac{mW}{s}$ for normalisation (without blood) and comparison (with blood and ratio)

C_{blood}	100 %	50 %	25 %	0 %
without blood	6.80	7.22	5.60	6.10
with blood	0.97	1.06	4.20	-
ratio	7.01	6.84	1.33	-

The fitted SR values of μ_{eff} are shown in Table 5.3. They are on the lower boundary compared to previous SR measurements on human prostate *in vivo* at $732nm$ ($\mu_{eff} = [0.9, 6.7]\ cm^{-1}$ with mean at $2.9 \pm 0.7\ cm^{-1}$ and $\mu_a = [0.07, 1.62]\ cm^{-1}$ with mean at $0.37 \pm 0.24\ cm^{-1}$) [30]. Previous time-resolved measurements [22] support the values in [30]. The reason for the low attenuation in the phantom might be a low content of Intralipid and therefore low μ_a. In this case, we are focusing on the attenuation by blood. The attenuation by the prostate is therefore a possible source of error that we can accept.

Table 5.3: Fitted μ_{eff} in cm^{-1} from SR measurements

C_{blood}	100 %	50 %	25 %	0 %
660 nm	0.9713	0.7315	0.8533	0.8486
786 nm	1.0428	0.9904	0.8339	0.9168
830 nm	1.1683	0.9671	0.9550	1.0337
916 nm	1.5005	1.4031	1.3265	1.5000

The average transmitted power per second in Table 5.2, $a_i P$, decreases with increased blood concentration. Furthermore, it varied somewhat depending on which sealed glass tube was used and because of laser fluctuations. It was measured as the mean of the whole wavelength spectrum wherefor the relative values of the blood concentrations give the mean blood attenuation. The exact values at individual wavelengths are found by taking the relative (y-axis) distance of the plots in Figure 5.1, according to Eq. 5.2. Since the lines are

not perfectly parallel, Δh is taken at $r = 8mm$. The amount of attenuation are therefore found with Eq. 5.3 and the damping, i.e. a_i^{-1}, are displayed in Table 5.4.

$$\Delta h = -\ln\frac{a_i\,P}{4\pi Dr} - (-\ln\frac{a_0\,P}{4\pi Dr}) = \ln\frac{a_0}{a_i} \tag{5.2}$$

$$a_i = a_0\,e^{-\Delta h} \tag{5.3}$$

Table 5.4: Damping factors, a_i^{-1}, per unit distance ($\approx 0.5mm$) relative to $C_{blood} = 0\%$ from SR measurements. Right column shows means recalculated to 100%, left bottom row shows regular means for the different blood concentrations, and right bottom cell shows recalculated mean of all a_i^{-1}.

C_{blood}	100 %	50 %	25 %	$\mu_\lambda(100\%)$
660 nm	8.5873	2.4247	1.2777	6.1825
786 nm	4.9635	3.6690	1.4794	6.0731
830 nm	5.4064	4.7545	1.6256	7.1393
916 nm	7.2399	6.8640	1.9429	9.5798
	6.5493	4.4281	1.5814	7.2 ± 2.5

5.3   Comparison of the results

The almost parallel lines in the SR measurements (Figure 5.1) indicate that μ_{eff} does not depend of blood at the fibre tip, but only on the wavelength. The small error bars ($\pm\sigma$) assure the quality of the measurements. The SR error of μ_{eff} for with to without blood is shown in the left part of Table 5.5. Compared to the TR measurements in Table 5.1, the SR values are generally higher as the positive errors in the right part of Table 5.5 indicate. Receiving lower values of μ_{eff} at TR with our setup is a reappearing observation. Of higher significance is that the discriminations between the wavelengths are small, which is confirmed by the errors to SR $C_{blood} = 0\%$ of less than 15% as seen in the left side of Table 5.5.

The damping factors in Table 5.4 that were found show slight indications of a pattern. The first value at $660nm$ and 100% does not fit, but otherwise the damping factor seems to increase with the wavelength. That is also observable for HbO_2 in Figure 2.1, but the evidence is not strong enough to base a conclusion on that.

The wavelength specific damping factors can be compared to the average transmitted power, which were measured with the separate calibration instrument. The ratio of the

Table 5.5: The (non-absolute) relative error, $\epsilon_\mu(approx, known) = \frac{\mu(approx) - \mu(known)}{\mu(known)}$ for SR blood and to TR measurement

	$\epsilon_\mu((SR, C_{blood}), (SR, C_{0\%}))$			$\epsilon_\mu((SR, C_{0\%}), (TR, C_{0\%}))$
C_{blood}	100 %	50 %	25 %	
660 nm	0.1445	-0.1381	0.0055	0.3781
786 nm	0.1374	0.0802	-0.0904	0.0910
830 nm	0.1302	-0.0645	-0.0762	0.2124
916 nm	0.0003	-0.0646	-0.1157	0.2134

power with to without blood are displayed on the last row in Table 5.2. Comparison shows good correspondence for 100% and 25%, while the 50% ratio of the average transmitted power seems to high.

To find an approximation of the damping, the values of Table 5.4 are recalculated to $C_{blood} = 100\%$ (factorised by 1, 2, and 4, respectively) in the right column of Table 5.4. In the bottom right cell, a crude approximation for the damping of these blood pools are found by taking the mean, giving $a_i^{-1} \approx 7.2 \pm 2.5$. As an even rougher estimate, the blood pools diameter is taken to be $1mm$, i.e. $0.5mm$ blood damping, wherefore a damping per mm is estimated to $a_i^{-1} \sim 15 \pm 5mm^{-1}$, which fits the values in [23].

CHAPTER 6

CONCLUSIONS

6.1 Fibre positioning

The algorithms tested provide excellent solutions within a reasonable time. In less than a minute, solutions were found that are better than the best random solutions found in 6 hours. That conclusion is based on the obtained fitness values in the fitness values figures, Figures 4.2, 4.5 and 4.8, compared to the distribution of random fitness values in Figure 4.1. The same parameters and classification3DModel were used etc. and the distribution looks almost Gaussian and is thereby only slightly biased (probably by the calculation of the positions). Especially the Random Search and the fast Simulated Annealing algorithm delivered high quality results quickly. Here, only data for comparison is presented, but the similar experiences have been made over and over again, but on different 3D models and with different parameters.

How good the fibre positions actually are distributed however depends mostly on the choice of the fitness function. Experience in what positions are the best would help that optimisation process. The spread of the positions were not that satisfactory for the high fitness values, as can be seen in Figures 4.3, 4.6 and 4.9. A larger distance between the positions would be expected, but this seems to be a general fact for many configurations with high fitness values. It should be possible to improve the spread by adding some term to the objective function.

The dose-volume histograms in Figures 4.4, 4.7 and 4.10 did not give much additional

information for the comparison. One could argue that the fast Simulated Annealing produces the highest tumour tissue treatment and still spares urethra better than the other two, but the differences are small. They however confirmed that all the obtained results were good, i.e. high tumour tissue treatment and low sensitive tissue exposure, especially for rectum but also for the sphincters. The objective function used, the regular fitness function, seems to be a good measure with regards to the DVH. The least squares fitness function did not deliver any good results, since it can not effectively be combined with multiple objectives.

Finally, the Matlab profiler was used to improve the code during the initial tests. Thereby the speed of the general calculations was optimised. Some major benefits in terms of speed were found by only using 25% of the tumour voxels and by ignoring normal tissue, see Table 4.2.

6.1.1   Future work

The parameters for the fitness function and for the algorithms could be further optimised. Some optimisation tools would come handy to make automatic parameter studies, since this is an extensive task. For the Random Step algorithm, the step sizes should be further studied. For fast Simulated Annealing, the step size could also be altered as well as the annealing scheme. In an interesting article on fast Simulated Annealing [16], Pouliot et al. discuss the clinical criteria for the objective function for brachytherapy seeds implant. The method presented builds the fitness function using a) a potential for minimum tumour dose, b) a potential for dose uniformity and c) limited dose to urethra and rectum. In our fitness function, b) has not been included, which would of course stimulate evenly spread positioning.

An alternative would be to use commercial software from brachytherapy adapted for IPDT, by e.g. MedCom or SonoTech. Since they are not open source, they are not easily adaptable to adjust for the difference in requirements. A major difference is that in IPDT there is no maximum dose to tumour requirement because of the finite oxygen supply.

6.2   Implications of blood pooling on IPDT dosimetry

If light transmitting a blood pool has a damping a_i^{-1} that is independent of the wavelength, it could become an important result for the improvement of IPDT. The comparisons made here,

indicate that blood pooling has only a slight wavelength dependent affect on the attenuation of light. This could be due to wavelength dependent absorption and/or scattering within the blood occlusion and is in need of further investigation. Table 5.5 shows errors in μ_{eff}, when exposed to blood, of less than 15%, i.e. μ_{eff} is left almost unaltered. A fibre trapped in the middle of a $1mm$ blood pool experienced damping of $a_i^{-1} \approx 7.2 \pm 2.5$ times and a very crude estimation of the average damping resulted in values of $a_i^{-1} \approx 15 \pm 5mm^{-1}$.

Sources of error in this experiment are predominantly of human nature. The adjustment of the fibre distance has to be right to get data that fits straight lines nicely as in Figure 5.1. The errors in μ_{eff} could be due to measurement inaccuracies as e.g. the 16 and $26mm$ outliers that can be seen in the 100% measurement. The fits presented here are not adjusted for outliers, wherefor we can conclude from the size of the error bars that some mistakes were made in the 25% and the 100% measurements. Another limiting factor would be the condition of the the bovine blood used for the blood pools. The blood was kept in cooled conditions for several days before the experiment. Prior to that, the butchery had had some salt solution poured into it for freshness, which could affect μ_{eff} as well as a_i.

A confirmation of these promising results was tried out at SpectraCure AB with the P18 system that is in use for IPDT treatment. 3 of the 18 fibres were applied with the same 100% bovine blood concentration tubes and another 3 with 50% ones. The system runs on $652nm$, wherefor results similar to the ones observed at $660nm$ were hoped for. A fibre positioning configuration from a previous treatment was used and the new phantom was added more intra lipid to resemble real conditions as much as possible. A major issue was the tight fibre positioning which in combination with the fluid prostate phantom made the system vulnerable for external impact, e.g. when adjusting the fibres. A more sophisticated evaluation method for occluded transmission data[1] was intended to find exact values of a_i and μ_{eff}. At first the results looked to be promising, with evenly distributed μ_{eff} and some fibres indicating damping. However, the in this case essential absolute calibration in combination with the movements of the fibre positions, caused that no certain conclusions could be made from that experiment, since results revealed evident inaccuracies.

6.2.1 Future work

A new attempt on the P18 experiment that was briefly reviewed here, could very well confirm the observations made earlier. If that is the case, it is essentially possible to make real-time

---

[1]Method in use for patient evaluation at SpectraCure AB

compensation for blood occlusion. Either a non-liquid phantom or a setup that allows for stability adjustment of the fibres would be helpful.

6.3   Final remarks

The most important result of this thesis would be that blood attenuation can be measured, with only a slight affect on μ_{eff}, i.e. less than 15% error, at more than 7 times damping. If this result can be confirmed by further measurements, it could have beneficial implications not only on IPDT, but also to other aspects of Bio-Photonics. Another final conclusion worth repeating, is that there seems to be several ways to efficiently and successfully optimise an objective function for IPDT, examples of those are the fast Simulated Annealing algorithm and the Random Step algorithm. However, to further improve the optimisation process, the objective function is of essential matter.

6.4   Acknowledgements

Most of all, I would like to thank Johannes Swartling, who supervised me throughout the work for this thesis and who was of great assistance in the documentation as well. I would also like to thank my supervisor at the Atomic Physics Department, Stefan Andersson-Engels, who was very helpful in the structuring of the work. Moreover, I would like to thank Johan Axelsson for great collaboration in the laboratory. Also, I would like to express my gratitude to the other people at SpectraCure AB, who made me feel welcome and made room for me, even though there was absolutely none left. Another appreciation goes out to Sjöbo slakteri, who generously donated bovine blood for cancer research. Finally I would like to thank the other people at the Medical Laser Physics Group, the research that you do there is really astonishing and I am proud to have had the opportunity to participate in it.

References

[1]. Ron Alterovitza, Etienne Lessard, Jean Pouliot, James F. OBrien, and Ken Goldberg. Optimization of hdr brachytherapy dose distributions using linear programming with penalty costs. *Med. Phys.*, 33(11):4012–4019, 2006.

[2]. Martin D. Altschuler, Timothy C. Zhu, Jun Li, and Stephen M. Hahn. Optimized interstitial pdt prostate treatment planning with the cimmino feasibility algorithm. *Med. Phys.*, 12(32):3524–3536, 2005.

[3]. Oscar Barajas, Åse M Ballangrud, Gerald G Miller, Ronald B Moore, and John Tulip. Monte carlo modelling of angular radiance in tissue phantoms and human prostate: Pdt light dosimetry. *Phys. Med. Biol.*, pages 1675–1687, 1997.

[4]. T.J. Dougherty, G.B. Grindey, R. Fiel, K.R. Weishaupt, and D.G. Boyle. Photoradiation therapy. ii. cure of animal tumors with hematoporphyrin and light. *J. Natl. Cancer Inst.*, 55:115–121, 1975.

[5]. Andreas Eriksson and Jonas Hjelm. Optimization of fibre positions in arbitrary tumour geometries for interstitial photodynamic therapy. Master's thesis, Lund University, Faculty of Engineering, 2004.

[6]. Ann Johansson. *Spectroscopic Techniques for Photodynamic Therapy Dosimetry*. PhD thesis, Lund University, Faculty of Engineering, 2007.

[7]. Ann Johansson, Johannes Swartling, Johan Axelsson, and Stefan Andersson-Engels. Realtime light dosimetry software tools for interstitial photodynamic therapy of the human prostate. *Physics in Medicine and Biology*, 34:4309–4321, 2007.

[8]. S. Kirkpatrick, Jr. C. D. Gelatt, and M. P. Vecchi. Optimization by simulated annealing. *Science*, 220(4598):671–680, 1983.

[9].   Etienne Lessard and Jean Pouliot. Inverse planning anatomy-based dose optimization for hdr-brachytherapy of the prostate using fast simulated annealing algorithm and dedicated objective function. *Med. Phys.*, 28(5):773–779, 2001.

[10]. R.L. Lipson, E.J. Baldes, and M.J. Gray. Hematoporphyrin derivative for detection and management of cancer. *Cancer*, 20:2255–2257, 1967.

[11]. A. Majeed, P. Babb, J. Jones, and M. Quinn. Trends in prostate cancer incidence, mortality and survival in england and wales 1971-1998. *BJU Int.*, 85(9):1058–1062, 2000. National Cancer Registration Bureau, Office for National Statistics, London, UK.

[12]. Tamaki Matsumoto1, Takahisa Ushiroyama, and Noriyuki Tatsumi. Lower peripheral circulation in eumenorrheic young women with premenstrual symptoms. *BioPsychoSocial Medicine , 1:8doi:10.1186/1751-0759-1-8*, 1, 2007.

[13]. F. Meyer-Betz. Untersuchungen über die biologische (photodynamische) wirkung des hämatoporphyrins und andere derivate des blut- und gallenfarbstoffs. *Dtsch. Arch. Klin. Med.*, 112:476–450, 1913.

[14]. Sven Påhlman. Hypoxiska solida tumörer blir aggresiva. *Onkologi i Sverige*, (3):72–74, 2007.

[15]. Sara Pålsson. *Methods, Instrumentation and Mechanisms for Optical Characterization of Tissue and Treatment of Malignant Tumours*. PhD thesis, Lund University, Faculty of Engineering, 2003.

[16]. Jean Pouliot, Daniel Tremblay, Jean Roy, and Santo Filice. Optimization of permanent [125]i prostate implants using fast simulated annealing. *International Journal of Radiation Oncology Biology and Physics*, 36(3):711–720, 1996.

[17]. William H. Press, Brian P. Flannery, Saul A. Teukolsky, and William T. Vetterling. Simulated annealing methods. In *Numerical recipes in C: The art of scientific computing*, pages 444–455. 1992.

[18]. O. Raab. Über die wirkung fluoreszierenden stoffe auf infusoria. *Zeitschrift für Biologie*, 39:524–546, 1900.

[19]. Drzymala R.E., Mohan R., Brewster L., Chu J., Goitein M., Harms W., and Urie M. Dose-volume histograms. *Int J Radiat Oncol Biol Phys.*, 1(21):71–78, 1991.

[20]. Ron S. Sloboda. Optimization of brachytherapy dose distributions by simulated annealing. *Med. Phys.*, 19(4):955–961, 1992.

[21]. D Souza, R Meyer, R Thomadsen, and C Ferris. An iterative sequential mixed-integer approach to automated prostate brachytherapy treatment plan optimization. *Phys. Med. Biol.*, 46:297–322, 2001.

[22]. Tomas Svensson, Stefan Andersson-Engels, Margrét Einarsdóttír, and Katarina Svanberg. In vivo optical characterization of human prostate tissue using near-infrared time-resolved spectroscopy. *Journal of Biomedical Optics*, 12(1), 2007.

[23]. Johannes Swartling. *Biomedical and atmospheric applications of optical spectroscopy in scattering media*. PhD thesis, Lund University, Faculty of Engineering, 2002.

[24]. Centre for Epidemiology The Swedish Cancer Registry. Cancer incidence in sweden 2006, Dec 2007. www.socialstyrelsen.se/Statistik.

[25]. H. von Tappeiner and A. Jesionek. Therapeutische versuche mit fluorescierenden stoffen. *Münch. Med. Wochenschr.*, 47:2042–2044, 1903.

[26]. H. von Tappeiner and A. Jodlbauer. *Die sensibiliserende Wirkung fluorescierender Substanzen. Gesammelte Untersuchungen uber die photodynamische Erscheinung.* FCW Vogel, 1907.

[27]. Helene Wallskär. Om psa-test. Cancerfonden, 2005. www.cancerfonden.se/templates/Information.

[28]. Ashley J. Welch and Martin J.C. van Gemert. *Optical-thermal response of laser-irradiated tissue.* Plenum Press, New York, 1995.

[29]. Sua Yoo, Michael E. Kowalok, Bruce R. Thomadsen, and Douglass L. A greedy heuristic using adjoint functions for the optimization of seed and needle configurations in prostate seed implant. *Physics in Medicine and Biology*, 52(3):815–828, 2007.

[30]. Timothy C. Zhu, Jarod C. Finlay, and Stephen M. Hahn. Determination of the distribution of light, optical properties, drug concentration, and tissue oxygenation in-vivo in human prostate during motexafin lutetium-mediated photodynamic therapy. *Journal of Photochemistry and Photobiology B: Biology*, (79):231–241, 2005.